

ARTICLE OPEN



Exciton–phonon interactions in nanocavity-integrated monolayer transition metal dichalcogenides

David Rosser¹, Taylor Fryett², Albert Ryou², Abhi Saxena² and Arka Majumdar^{1,2}✉

Cavity-integrated transition metal dichalcogenide (TMDCs) excitons have recently emerged as a promising platform to study strong light–matter interactions and related cavity quantum electrodynamics phenomena. Although this exciton–cavity system is typically modeled as coupled harmonic oscillators, to account for the rich solid-state environment, the effect of exciton–phonon interaction needs to be incorporated. We model the system by including a phenomenological deformation potential for exciton–phonon interactions and we elucidate the experimentally measured preferential coupling of the excitonic photoluminescence to the cavity modes red-detuned with respect to the exciton resonance. Furthermore, we predict and experimentally confirm the temperature dependence of this preferential coupling. By accurately capturing the exciton–phonon interaction, our model illuminates the potential of cavity-integrated TMDCs for the development of low-power classical and quantum technologies.

npj 2D Materials and Applications (2020)4:20; <https://doi.org/10.1038/s41699-020-0156-9>

INTRODUCTION

Atomically thin van der Waals materials have recently emerged as a promising platform for engineering novel light–matter interactions^{1–3}. Among various van der Waals materials, the semiconducting transition metal dichalcogenides (TMDCs) allow for the robust exploration of cavity quantum electrodynamics (cQED) in an ostensibly scalable system by their direct integration with on-chip, planar nanophotonic cavities^{3,4}. In this hybrid system, the TMDC excitons evanescently couple to the photonic modes. Several recent studies have reported cavity integration of these materials exhibiting optically pumped lasing^{5–8}, cavity enhanced second harmonic generation^{9,10}, cavity enhanced electroluminescence¹¹, and strong coupling¹². Beyond these demonstrations, there exist theoretical proposals utilizing TMDC excitons for quantum optical applications in single photon non-linear optics^{13,14}.

A necessary step for elucidating the potential applications of cavity-integrated TMDCs is an understanding of the relevant underlying physics of the exciton–cavity interaction. The prevailing description of the interaction between TMDC excitons and quantum optical cavity modes largely neglects the role of the solid-state environment. However, exciton–phonon interactions are known to have a significant effect on the neutral exciton photoluminescence (PL)^{15–21}. In other solid-state cQED systems, such as self-assembled quantum dots coupled to nanocavities, the exciton–phonon interaction is known to cause an asymmetric photoluminescent lineshape in the form of phonon sidebands, as well as modify the cavity-coupled PL^{22–24}. In addition, after a careful review of the published literature on TMDCs coupled to whispering gallery mode resonators, we find multiple instances where the exciton’s PL emission into the cavity modes appear preferentially coupled to the red-detuned side of the exciton resonance^{6,7,25,26}. This intriguing asymmetric coupling between the excitons and the cavity modes, which is not predicted by the simple coupled oscillator exciton–cavity theory, points to an important missing parameter in the model.

In this paper, we investigate the role of acoustic phonons in the coupling of monolayer TMDCs to nanophotonic resonators. Coupling of the TMDC neutral exciton to a cavity mode is represented as coupled oscillators within the rotating wave approximation^{14,27} and a deformation potential is used to model the exciton–phonon interaction^{28,29}, similar to the studies in self-assembled quantum dots coupled to nanocavities. An effective master equation is employed to describe phonon-mediated decay processes and incoherent exciton–cavity coupling³⁰. Experimentally, we placed monolayer WSe₂ onto a silicon nitride ring resonator, which allows for the simultaneous measurement of multiple cavity modes at different detunings. Our model exhibits preferential coupling of the exciton emission to red-detuned cavity modes, faithfully reproducing the experimental data. We further validate the theoretical model with a prediction and experimental confirmation that the asymmetry decreases with increasing temperature.

RESULTS

Polaron master equation

A homogenous distribution of TMDC excitons and a single, dispersionless cavity mode is typically formulated in terms of a coupled oscillator model H_{XC} , wherein the exciton and cavity coherently interact via an exciton–cavity coupling $\hbar g$ ^{14,27}. The resonance frequency can be measured with respect to a rotating frame at the resonant drive frequency ω_L . The deformation potential exciton–phonon interaction H_{XP} ^{28,29} is similar to that seen in the spin-boson model^{31,32} or for optomechanical systems³³, where the exciton number operator is coupled to a bath of harmonic oscillators b_q with frequency ω_q and coupling λ_q . Thus, the coupled system is described by the Hamiltonian $H = H_{XC} + H_{XP}$

$$H_{XC} = \hbar\Delta_{XL}a^\dagger a + \hbar\Delta_{CL}c^\dagger c + \hbar g(a^\dagger c + c^\dagger a)$$

$$H_{XP} = \hbar a^\dagger a \sum_q \lambda_q (b_q + b_q^\dagger) + \sum_q \hbar \omega_q b_q^\dagger b_q$$

¹Department of Physics, University of Washington, Seattle, WA 98195, USA. ²Department of Electrical and Computer Engineering, University of Washington, Seattle, WA 98195, USA. ✉email: arka@uw.edu

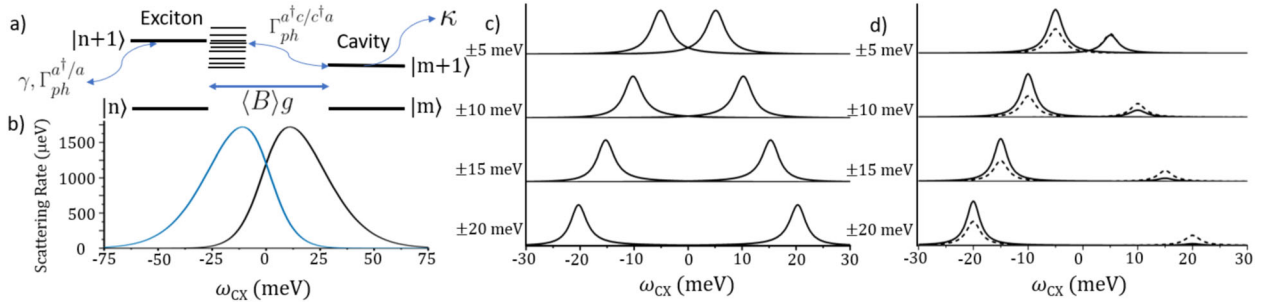


Fig. 1 Exciton-cavity detuning-dependent phonon-mediated scattering. Theoretical modeling with the Hamiltonian described in the text ($T = 80$ K, $\gamma = 48.4$ meV, $a_p = 0.018$ ps², $\omega_b = 6.7$ meV, $\kappa = 2.85$ meV, $g = 4$ meV). **a** Level diagram with phonon-mediated scattering. **b** Asymmetric phonon-mediated exciton-cavity coupling rates. The blue line gives the phonon-mediated incoherent emission into the cavity. Note that the peak is not centered at zero detuning. **c** Detuning dependent ($\Delta_{CX} = \pm 5, \pm 10, \pm 15, \pm 20$ meV) cavity emission without phonons. **d** Detuning-dependent cavity emission with phonons at 80 K (solid line) and 320 K (dashed line). Note that for the $\Delta_{CX} = +5$ meV the dashed and solid line are on top of each other for the blue-detuned case.

where $\Delta_{XL} = \omega_X - \omega_L$ and $\Delta_{CL} = \omega_C - \omega_L$ are the detunings of the exciton and the cavity from the laser wavelength, respectively; a (c) is the annihilation operator for the exciton (cavity) mode. In the weak excitation regime, we neglect exciton saturation and any exciton–exciton interaction. Hence, we can treat both exciton and cavity operators as bosonic.

In order to distinguish the observed neutral exciton from the effects associated with phonon bath induced fluctuations, we use the polaron transformation $P = a^\dagger a \sum_q \frac{\lambda_q}{\omega_q} (b_q^\dagger - b_q)$ with $H \rightarrow e^P H e^{-P}$ ³⁴, which leads to the system Hamiltonian (Supplementary Note 1)^{31,33,35,36}

$$H'_S = \hbar(\Delta_{XL} - \Delta_P)a^\dagger a - \hbar\Delta_P a^\dagger a^\dagger a a + \hbar\Delta_{CL}c^\dagger c + \hbar\langle B \rangle g(\sigma^+ a + a^\dagger \sigma^-) \quad (1)$$

The exciton resonance $\Delta' = \Delta_{XL} - \Delta_P$ is renormalized by a polaron shift $\Delta_P = \sum_q \frac{\lambda_q^2}{\omega_q}$, which is analogous to a Lamb shift³⁷. When the harmonic oscillator bath is written in terms of the phonon displacement operator $B_\pm = \exp[\pm \sum_q \frac{\lambda_q}{\omega_q} (b_q - b_q^\dagger)]$ the exciton-cavity coupling is modified from the bare value by the average phonon displacement $\langle B \rangle$

$$\langle B \rangle = \exp\left[-\frac{1}{2} \sum_q \left(\frac{\lambda_q}{\omega_q}\right)^2 (2\bar{n}_q + 1)\right]$$

where $\bar{n}_q = [e^{\beta\hbar\omega_q} - 1]^{-1}$ is the mean phonon number with bath temperature $T = 1/k_B\beta$ ³⁸. As the temperature increases, the average phonon number in each mode increases, which decreases the exciton-cavity interaction.

We employ an effective master equation $\frac{\partial \rho}{\partial t} = \frac{1}{\hbar}[H', \rho] + \frac{\kappa}{2}\mathcal{L}[c] + \frac{\gamma}{2}\mathcal{L}[a] + \frac{\Gamma_{ph}^{a^\dagger c}}{2}\mathcal{L}[a^\dagger c] + \frac{\Gamma_{ph}^{c^\dagger a}}{2}\mathcal{L}[c^\dagger a]$ (Supplementary Note 2)³⁰ to model the incoherent exciton-cavity feeding. Figure 1a illustrates the energy-level diagram of the exciton and cavity system. The dissipator $\mathcal{L}[\xi] = \xi\rho\xi^\dagger - \frac{1}{2}\xi^\dagger\xi\rho - \frac{1}{2}\rho\xi^\dagger\xi$ with Lindblad operators ξ describes the cavity decay rate (κ), exciton decay rate (γ), and the incoherent phonon-mediated exciton-cavity scattering ($\Gamma_{ph}^{a^\dagger c}, \Gamma_{ph}^{c^\dagger a}$).

The phonon-mediated exciton-cavity scattering (Fig. 1b) with cavity-exciton detuning $\Delta_{CX} = \omega_C - \omega_X$ is given by

$$\Gamma_{ph}^{a^\dagger c/c^\dagger a} = 2\langle B \rangle^2 g^2 \text{Re}\left[\int_0^\infty dt e^{\pm\Delta_{CX}\tau} (e^{\phi(\tau)} - 1)\right] \quad (2)$$

with the phonon correlation function $\phi(\tau) = \int_0^\infty d\omega \frac{J(\omega)}{\omega^2} [\cot h(\frac{\hbar\omega}{2k_B T}) \cos(\omega\tau) - i \sin(\omega\tau)]$ ^{31,39}. We assume a Gaussian localization of the exciton confined to the monolayer TMDC owing to substrate inhomogeneities coupled to acoustic phonons for a qualitative super-ohmic spectral density

$J(\omega) = a_p \omega^3 \exp(-\omega^2/2\omega_b^2)$ ^{28,31} with a_p and ω_b serving as the exciton–phonon coupling strength and cutoff frequency, respectively. This phonon spectral function is identical to that used in quantum dot studies of phonon interactions^{36,40,41}.

Without phonon-mediated scattering, the peak cavity intensity occurs at zero detuning ($\omega_C = \omega_X$) and the cavity-coupled PL is symmetric with respect to the exciton PL emission peak (Fig. 1c). The additional scattering from phonon processes of the exciton into the cavity mode dominates when the cavity is red-detuned with respect to the exciton (Fig. 1d). Physically, we expect down-conversion of an exciton into a phonon and cavity photon as an example of a Stokes process. The opposite up-conversion amounts to optical refrigeration⁴². Including phonon-mediated scattering demonstrates the peak cavity intensity is red-detuned with respect to the exciton PL emission peak. Furthermore, our model predicts that at the same detuning, the relative intensity between the red-detuned and blue-detuned cavity-coupled PL decreases for increasing temperature (Fig. 1d, dashed line)³⁰.

Exciton-cavity PL spectra

To validate our quantum optical model, we performed experiments with a ring resonator integrated with a monolayer of WSe₂. A ring resonator can support multiple cavity modes separated by the free spectral range, and thus provides an ideal platform for studying the coupling of the PL to cavity modes with different detunings from the exciton.

The transmission spectrum of the SiN ring resonator is measured by exciting a grating coupler with a supercontinuum laser (Fianium WhiteLase Micro) and collecting from the other grating coupler (Fig. 2a, inset). An initial transmission measurement of the ring resonator before monolayer TMDC transfer yields the bare cavity linewidth of $\kappa = 2.85$ meV (Fig. 2b). The dips in the transmission correspond to the resonance in the ring resonators. The separation between the modes corresponds to the free spectral range ($\text{FSR} = \frac{c}{2\pi n_{\text{eff}} R} \approx 4.8$ THz) of the ring resonator, which matches the FSR expected from the ring radius ($R = 5$ μm) and effective index of refraction of the SiN waveguide ($n_{\text{eff}} \approx 2$). The envelope modulation of the spectrum is owing to the frequency-dependent coupling efficiency of the grating couplers (Fig. 2b, c). The angular dependence of the grating coupler does not affect the cavity-coupled PL measurement owing to the large numerical aperture of our objective lens. There exists a relative amplitude change between the envelope modulation function in the observed transmission spectrum owing to the angular dependence of the grating couplers. As the measurement is done before and after the transfer, which requires removing the sample from the optical setup, the angular alignment of the confocal microscope objective to the grating coupler will be slightly

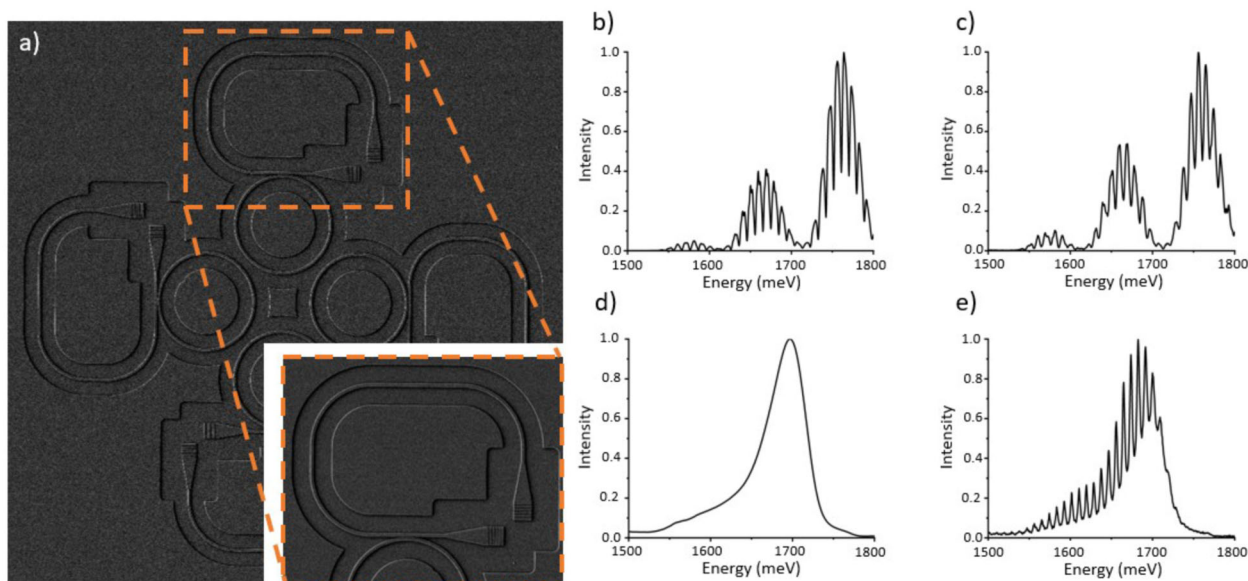


Fig. 2 Photoluminescence and transmission spectra. **a** SEM of four 5 μm (radius) uncoupled SiN ring resonators. Inset: SEM of the coupled ring/waveguide and grating couplers. The grating couplers are used to input light and collect transmitted light. **b** Transmission spectrum of the SiN ring resonator before integration of monolayer WSe₂. **c** Transmission spectrum of the SiN ring resonator after integration of monolayer WSe₂. **d** PL of monolayer WSe₂. **e** Cavity-coupled PL of monolayer WSe₂.

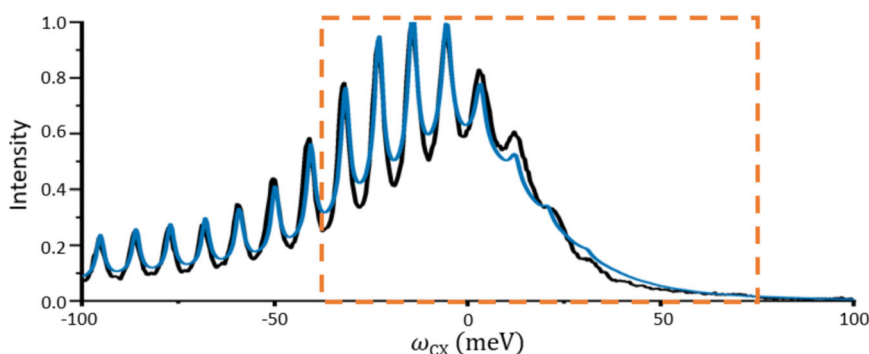


Fig. 3 Theoretical fit of a polaron model to cavity-coupled photoluminescence data. Measured cavity-coupled PL (black) and simulated cavity-coupled PL (blue) at 80 K. Theoretical model fit to the windowed region of data with the Hamiltonian described in the text ($T = 80$ K, $\gamma = 48.4$ meV, $a_p = 0.018$ ps², $\omega_b = 6.7$ meV, $\kappa = 2.85$ meV, $g = 4$ meV).

different⁴³. The transmission spectrum of the ring resonator after material transfer demonstrates the monolayer does not significantly affect the cavity modes (Fig. 2c). It is important to point out that with the exciton at ~ 1700 meV, the small linewidth increase seen in the transmission spectrum equally affects cavity modes both red and blue-detuned with respect to the exciton resonance.

PL was first measured to confirm the existence of the monolayer after material transfer because 2D materials exhibit poor optical contrast on the SiN substrate (Fig. 2d). The strong excitonic peak of the WSe₂ monolayer integrated onto the SiN ring resonator establishes the presence of the vdW material on the waveguide⁴⁴. The primary peak is attributed to neutral exciton emission. The secondary sidebands could be owing to defects or trion emission^{45,46}. PL is measured by exciting the monolayer with a HeNe laser (40 μW at 633 nm). By fitting the measured PL at 80 K, the material-dependent parameters for the phonon spectral function can be calculated, independent of the cavity coupling (Supplementary Note 3, Supplementary Fig. 1). We found an exciton linewidth $\gamma = 48.4$ meV, an exciton–phonon coupling $a_p = 0.018$ ps², and cutoff frequency $\omega_b = 6.7$ meV. These extracted parameters are consistent with values estimated from bulk material measurements. The polaron shift of the exciton energy

is then calculated to be $\hbar\Delta_p = \hbar \int_0^\infty d\omega J(\omega)/\omega = \hbar \sqrt{\pi/2} a_p \omega_b^3 = 24$ meV, which we incorporate into the modified exciton resonance $\Delta' = \Delta_{xl} - \Delta_p$.

Cavity-coupled PL is measured by directly exciting the monolayer WSe₂ from the top and collecting the resulting emission from a grating coupler using a pinhole in the image plane of a free-space confocal microscope. Cavity-coupled PL exhibits asymmetric emission into the cavity modes where there is greater intensity in the cavities red-detuned with respect to the exciton (Fig. 2e). The coherent exciton-cavity coupling $\hbar g$ can be extracted by considering the linear superposition of all cavity resonances for the ring resonator and including a contribution from background PL that is difficult to completely remove owing to the proximity of the grating coupler and laser excitation of the monolayer WSe₂. The exciton-cavity coupling accounting for the average phonon displacement is found to be $\hbar g \approx 4 - 6$ meV (Fig. 3) by a brute force search minimizing the least squares error between the simulated and observed data over a windowed region of the cavity-coupled PL spectrum. The far red-detuned data attributed to defect and trion emission was accounted for by a convolution of the PL and Lorentzian cavity modes (Supplementary Note 4). In this experiment only $\sim 1/4$ of the SiN ring

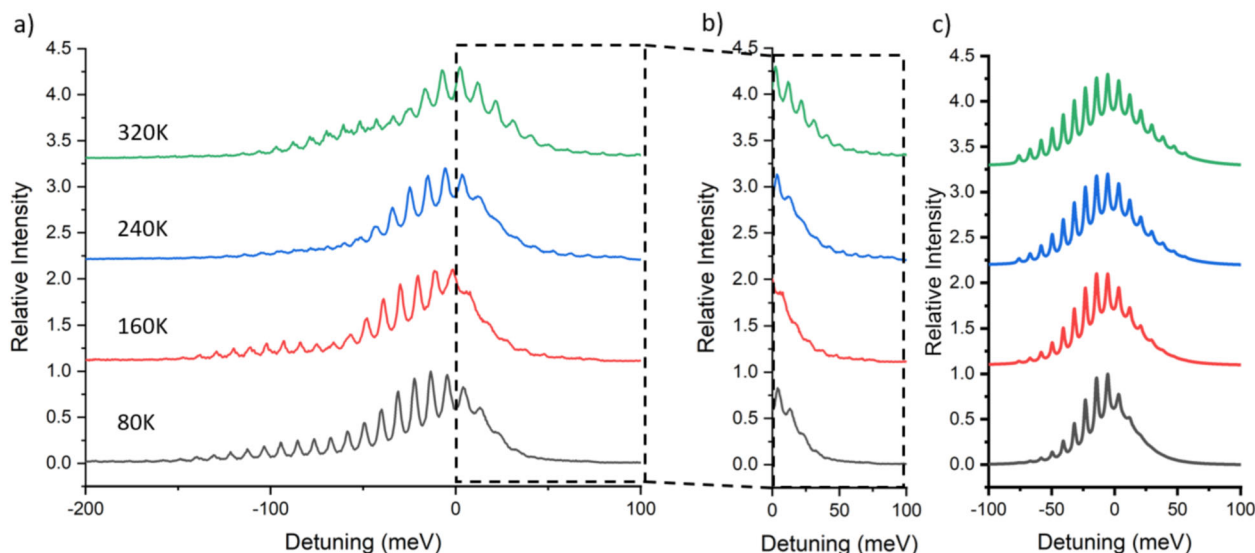


Fig. 4 Temperature-dependent cavity-coupled photoluminescence data and simulations. a Temperature dependence (80–320 K) of the asymmetric cavity-coupled PL. **b** Zoomed-in to show the temperature dependence of the asymmetric cavity-coupled PL for cavities blue-detuned with respect to the exciton. **c** Simulated temperature dependence of cavity-coupled PL without trion and defect emission. All free parameters are held fixed except the measured cryostat temperature ($T = 80$ K, 160 K, 240 K, 320 K, $\gamma = 48.4$ meV, $a_p = 0.018$ ps², $\omega_b = 6.7$ meV, $\kappa = 2.85$ meV, $g = 4$ meV).

resonator was covered with monolayer WSe₂. A full coverage of monolayer WSe₂ on the SiN ring resonator gives $\hbar g \approx 8 - 12$ meV as an estimated coherent interaction of the exciton and cavity mode owing to the $g \propto \sqrt{N}$ scaling of the light–matter interaction in the collective excitation basis and assuming the number of available exciton states is proportional to the area of monolayer material on the cavity. Our extracted g value is consistent with the light–matter interaction $\hbar g \approx 10 - 14$ meV found in strong-coupling experiments with van der Waals materials integrated on photonic crystal cavities with comparable length of the cavity^{12,47,48}. We note that for the ring resonator, the length of the cavity that goes into calculation of the $\hbar g$ is the thickness of the slab (~220 nm).

To further confirm the theoretical model, we measure the temperature-dependent variation in the asymmetric coupling in the range 80–320 K. Using liquid nitrogen in a continuous flow cryostat (Janis ST-500) we can tune the energy of the exciton in the monolayer WSe₂ from 1650–1700 meV with the consequent changes in linewidth. As the cryostat temperature is increased, we see cavity-coupled PL extending to further blue-detuned cavities with respect to the exciton energy (Fig. 4a) where the spectra are shifted by the exciton center frequency. In particular, the maximum detuning with visible cavity modes increases with increasing temperature (Fig. 4b). We find the model Hamiltonian parameters extracted from the PL and cavity-coupled PL qualitatively reproduce the spectrum at elevated temperatures (Fig. 4c) where the only modified simulation parameter is the measured temperature of the cryostat. Reduced asymmetry in cavity-coupled PL at elevated temperatures is owing to the reduced asymmetry of the phonon-mediated exciton-cavity coupling rates with respect to the neutral exciton resonance.

DISCUSSION

We have explored exciton–phonon interactions in cavity-integrated TMDCs and demonstrated that a phenomenological deformation potential has significant value in explaining asymmetric cavity emission^{6,7,25,26}. Reflecting on the effective system Hamiltonian (Eq. (1)), the polaron shift $\hbar\Delta_p = 24$ meV of the exciton energy is comparable to the polaron $\hbar\Delta_p = 29$ meV found via the excitonic Bloch equations¹⁹. Temperature dependence of

the exciton-cavity coupling has been previously observed in strong-coupling experiments with TMDC excitons^{12,48,49}, although a rigorous model explaining this behavior was not reported. We attribute this modification of the bare value to the average phonon displacement $g \rightarrow \langle B \rangle g$. A consequence of the exciton-cavity incoherent scattering (Eq. (2)) is an efficient means for exciton population inversion, which could potentially explain observations of lasing in cavity-integrated monolayer materials^{5–8,30,50}. In the interest of a low-power optical non-linearity, polaron–polaron scattering in the effective system Hamiltonian ($\Delta_p a^\dagger a^\dagger a a$) provides an interesting opportunity, which could lead to non-classical light generation³³. The calculated polaron shift is two orders of magnitude larger than expected for exciton–exciton scattering owing to a lateral confining potential¹⁴. A full understanding of the many-body interactions in nanocavity-integrated monolayer TMDCs is a necessary prerequisite to assessing the potential of this system for future classical and quantum technologies.

METHODS

Sample fabrication

The ring resonator is fabricated using a 220-nm-thick silicon nitride (SiN) membrane grown via low pressure chemical vapor deposition on 4 μm of thermal oxide on silicon. We spun ~400 nm of Zeon ZEP520A, which was coated with a thin layer of Pt/Au that served as a charging layer. The resist was patterned using a JEOL JBX6300FX electron-beam lithography system with an accelerating voltage of 100 kV. The pattern was transferred to the SiN using a reactive ion etch in CHF₃/O₂ chemistry. The mechanically exfoliated WSe₂ was then transferred onto the SiN ring resonator (Fig. 2a) using a modified dry transfer method to eliminate bulk material contamination²⁶, which would otherwise quench the optical properties of the waveguide structures.

DATA AVAILABILITY

The data that support the findings of this study are available from the corresponding author upon reasonable request.

CODE AVAILABILITY

The code that support the findings of this study are available from the corresponding author upon reasonable request.

Received: 29 February 2020; Accepted: 12 June 2020;
Published online: 10 July 2020

REFERENCES

- Xia, F., Wang, H., Xiao, D., Dubey, M. & Ramasubramaniam, A. Two-dimensional material nanophotonics. *Nat. Photon.* **8**, 899–907 (2014).
- Liu, Y. et al. Van der Waals heterostructures and devices. *Nat. Rev. Mater.* **1**, 16042 (2016).
- Liu, C.-h., Zheng, J., Chen, Y., Fryett, T. & Majumdar, A. Van der Waals materials integrated nanophotonic devices [Invited]. *Opt. Mater. Express* **9**, 384–399 (2019).
- Fryett, T., Zhan, A. & Majumdar, A. Cavity nonlinear optics with layered materials. *Nanophotonics* **7**, 355–370 (2018).
- Wu, S. et al. Monolayer semiconductor nanocavity lasers with ultralow thresholds. *Nature* **520**, 69–72 (2015).
- Ye, Y. et al. Monolayer excitonic laser. *Nat. Photon.* **9**, 733–737 (2015).
- Salehzadeh, O., Djalili, M., Tran, N. H., Shih, I. & Mi, Z. Optically pumped two-dimensional MoS₂ lasers operating at room-temperature. *Nano Lett.* **15**, 5302–5306 (2015).
- Li, Y. et al. Room-temperature continuous-wave lasing from monolayer molybdenum ditelluride integrated with a silicon nanobeam cavity. *Nat. Nanotechnol.* **12**, 987–992 (2017).
- Fryett, T. K. et al. Silicon photonic crystal cavity enhanced second-harmonic generation from monolayer WSe₂. *2D Mater.* **4**, 16042 (2016).
- Gan, X.-T. et al. Microwatts continuous-wave pumped second harmonic generation in few- and mono-layer GaSe. *Light Sci. Appl.* **7**, 17126–17126 (2018).
- Liu, C.-H. et al. Nanocavity integrated van der Waals heterostructure light-emitting tunneling diode. *Nano Lett.* **17**, 200–205 (2017).
- Zhang, L., Gogna, R., Burg, W., Tutuc, E. & Deng, H. Photonic-crystal exciton-polaritons in monolayer semiconductors. *Nat. Commun.* **9**, 1–8 (2018).
- Walther, V., John, R. & Pohl, T. Giant optical nonlinearities from Rydberg excitons in semiconductor microcavities. *Nat. Commun.* **9**, 1–6 (2018).
- Ryou, A., Rosser, D., Saxena, A., Fryett, T. & Majumdar, A. Strong photon antibunching in weakly nonlinear two-dimensional exciton-polaritons. *Phys. Rev. B* **97**, 16042 (2018).
- Moody, G. et al. Intrinsic homogeneous linewidth and broadening mechanisms of excitons in monolayer transition metal dichalcogenides. *Nat. Commun.* **6**, 1–6 (2015).
- Robert, C. et al. Exciton radiative lifetime in transition metal dichalcogenide monolayers. *Phys. Rev. B* **93**, 16042 (2016).
- Cadiz, F. et al. Excitonic linewidth approaching the homogeneous limit in MoS₂-based van der Waals heterostructures. *Phys. Rev. X* **7**, 16042 (2017c).
- Ajayi, O. A. et al. Approaching the intrinsic photoluminescence linewidth in transition metal dichalcogenide monolayers. *2D Mater.* **4**, 16042 (2017).
- Christiansen, D. et al. Phonon sidebands in monolayer transition metal dichalcogenides. *Phys. Rev. Lett.* **119**, 16042 (2017).
- Shree, S. et al. Observation of exciton-phonon coupling in MoSe₂ monolayers. *Phys. Rev. B* **98**, 16042 (2018).
- Glazov, M. M. Phonon wind and drag of excitons in monolayer semiconductors. *Phys. Rev. B* **100**, 16042 (2019).
- Majumdar, A., Kim, E. D., Gong, Y., Bajcsy, M. & Vučković, J. Phonon mediated off-resonant quantum dot–cavity coupling under resonant excitation of the quantum dot. *Phys. Rev. B* **84**, 16042 (2011).
- Englund, D. et al. Resonant excitation of a quantum dot strongly coupled to a photonic crystal nanocavity. *Phys. Rev. Lett.* **104**, 16042 (2010).
- Ates, S. et al. Non-resonant dot–cavity coupling and its potential for resonant single-quantum-dot spectroscopy. *Nat. Photonics* **3**, 724–728 (2009).
- Javerzac-Galy, C. et al. Excitonic emission of monolayer semiconductors near-field coupled to high-Q microresonators. *Nano Lett.* **18**, 3138–3146 (2018).
- Rosser, D., Fryett, T., Saxena, A., Ryou, A. & Majumdar, A. High-precision local transfer of van der Waals materials on nanophotonic structures. *Opt. Mater. Express* **10**, 645–652 (2020).
- Carreño, J. C. L. & Laussy, F. P. Excitation with quantum light. I. Exciting a harmonic oscillator. *Phys. Rev. A* **94**, 16042 (2016).
- Takagahara, T. Localization and energy transfer of quasi-two-dimensional excitons in GaAs-AlAs quantum-well heterostructures. *Phys. Rev. B* **31**, 6552–6573 (1985).
- Singh, J. *Excitation Energy Transfer Processes in Condensed Matter: Theory and Applications*. (Springer US, 1994).
- Hughes, S. & Carmichael, H. J. Phonon-mediated population inversion in a semiconductor quantum-dot cavity system. *N. J. Phys.* **15**, 16042 (2013).
- Leggett, A. J. et al. Dynamics of the dissipative two-state system. *Rev. Mod. Phys.* **59**, 1–85 (1987).
- Wilson-Rae, I. & Imamoglu, A. Quantum dot cavity-QED in the presence of strong electron-phonon interactions. *Phys. Rev. B* **65**, 16042 (2002).
- Rabl, P. Photon blockade effect in optomechanical systems. *Phys. Rev. Lett.* **107**, 16042 (2011).
- Merrifield, R. E. Theory of the vibrational structure of molecular exciton states. *J. Chem. Phys.* **40**, 445–450 (1964).
- Mahan, G. D. *Many-Particle Physics*. 3rd edn (Springer US, 2000).
- Roy, C. & Hughes, S. Polaron master equation theory of the quantum-dot Mollow triplet in a semiconductor cavity-QED system. *Phys. Rev. B* **85**, 16042 (2012).
- Roy-Choudhury, K. & Hughes, S. Quantum theory of the emission spectrum from quantum dots coupled to structured photonic reservoirs and acoustic phonons. *Phys. Rev. B* **92**, 16042 (2015).
- Roy, C. & Hughes, S. Influence of electron–acoustic-phonon scattering on intensity power broadening in a coherently driven quantum-dot–cavity system. *Phys. Rev. X* **1**, 16042 (2011).
- McCutcheon, D. P. S. & Nazir, A. Quantum dot Rabi rotations beyond the weak exciton–phonon coupling regime. *N. J. Phys.* **12**, 16042 (2010).
- Calarco, T., Datta, A., Fedichev, P., Pazy, E. & Zoller, P. Spin-based all-optical quantum computation with quantum dots: Understanding and suppressing decoherence. *Phys. Rev. A* **68**, 16042 (2003).
- Nazir, A. Photon statistics from a resonantly driven quantum dot. *Phys. Rev. B* **78**, 16042 (2008).
- Jones, A. M. et al. Excitonic luminescence upconversion in a two-dimensional semiconductor. *Nat. Phys.* **12**, 323–327 (2016).
- Chrostowski, L. & Hochberg, M. *Silicon Photonics Design*. (Cambridge Core, 2015).
- Chernikov, A. et al. Exciton binding energy and nonhydrogenic rydberg series in monolayer WS₂. *Phys. Rev. Lett.* **113**, 16042 (2014).
- Chow, P. K. et al. Defect-induced photoluminescence in monolayer semiconducting transition metal dichalcogenides. *ACS Nano* **9**, 1520–1527 (2015).
- Sidler, M. et al. Fermi polaron-polaritons in charge-tunable atomically thin semiconductors. *Nat. Phys.* **13**, 255–261 (2017).
- Dufferwiel, S. et al. Exciton-polaritons in van der Waals heterostructures embedded in tunable microcavities. *Nat. Commun.* **6**, 1–7 (2015).
- Kravtsov, V. et al. Nonlinear polaritons in monolayer semiconductor coupled to optical bound states in the continuum. *Light Sci. Appl.* **9**, 56 (2020).
- Liu, X. et al. Control of coherently coupled exciton polaritons in monolayer tungsten disulphide. *Phys. Rev. Lett.* **119**, 16042 (2017).
- Lohof, F. et al. Prospects and limitations of transition metal dichalcogenide laser gain materials. *Nano Lett.* **19**, 210–217 (2019).

ACKNOWLEDGEMENTS

The research was supported by NSF-1845009, NSF-ECCS-1708579, and AFOSR grant FA9550-17-C-0017. Part of this work was conducted at the Washington Nanofabrication Facility/Molecular Analysis Facility, a National Nanotechnology Coordinated Infrastructure (NNCI) site at the University of Washington, which is supported in part by funds from the National Science Foundation (awards NNCI-1542101, 1337840, and 0335765), the National Institutes of Health, the Molecular Engineering & Sciences Institute, the Clean Energy Institute, the Washington Research Foundation, the M.J. Murdock Charitable Trust, Altatech, ClassOne Technology, GCE Market, Google and SPTS. A.R. acknowledges support from the IC Postdoctoral Research Fellowship.

AUTHOR CONTRIBUTIONS

David Rosser conducted the experiment, simulations, and performed the data analysis. Taylor Fryett fabricated the ring resonator device. Albert Ryou, Abhi Saxena, and Arka Majumdar offered useful discussion.

COMPETING INTERESTS

The authors declare no competing interests.

ADDITIONAL INFORMATION

Supplementary information is available for this paper at <https://doi.org/10.1038/s41699-020-0156-9>.

Correspondence and requests for materials should be addressed to A.M.

Reprints and permission information is available at <http://www.nature.com/reprints>

Publisher's note Springer Nature remains neutral with regard to jurisdictional claims in published maps and institutional affiliations.



Open Access This article is licensed under a Creative Commons Attribution 4.0 International License, which permits use, sharing, adaptation, distribution and reproduction in any medium or format, as long as you give

appropriate credit to the original author(s) and the source, provide a link to the Creative Commons license, and indicate if changes were made. The images or other third party material in this article are included in the article's Creative Commons license, unless indicated otherwise in a credit line to the material. If material is not included in the article's Creative Commons license and your intended use is not permitted by statutory regulation or exceeds the permitted use, you will need to obtain permission directly from the copyright holder. To view a copy of this license, visit <http://creativecommons.org/licenses/by/4.0/>.

© The Author(s) 2020